AW09 TAIL ROTOR SYSTEM CONTROL AUTHORITY ASSESSMENT

Sören Bölk[1] Flight Performance Analysis Engineer
Alessandro Masi[1] Flight Mechanics Analysis Engineer
Francesco Scorcelletti[1] Team Leader Flight Mechanics and Performance

[1] Kopter Group AG, Wetzikon, Switzerland

Abstract

The tail rotor of a helicopter plays a crucial role in maintaining stability and control during flight. Therefore, it is essential to meet several performance and controllability requirements to ensure safe and efficient operation. One of these requirements is providing sufficient yaw control authority to enable the pilot to maneuver the helicopter effectively. However, specific challenges arise when dealing with a ducted tail rotor, such as the one installed in the AW09 helicopter—an innovative multi-role single-engine aircraft currently under development at Kopter Group AG. The current approach to modeling the yaw control authority involves calculating the tail rotor thrust using a commercial tool in a full aircraft model. Subsequently, the simulation of the tail rotor blade pitch and the corresponding pedal control demand is performed using an in-house developed code. The decision to develop a dedicated code for the tail rotor was made to ensure maximum modeling flexibility and tuning capabilities, enabling accurate replication of the behavior of the AW09 ducted rotor. In this paper, we present the methodology that combines a dedicated rotor analysis tool with the commercially available software, FLIGHTLAB, to verify the AW09 tail rotor system against a series of helicopter certification and operational requirements. Due to data confidentiality, the figures in the results section are presented without scales.

1 NOMENCLATURE

c	m	Blade chord
c_d	$-$	Sectional drag coefficient
c_l	$-$	Sectional lift coefficient
C_P	$-$	Power coefficient
C_T	$-$	Thrust coefficient
D	N	Drag force
f_T	$-$	Thrust share factor
$f_{V_{\mathrm{x,y,z}}}$	$-$	Free-stream correction factors
F_{n}	N	Axial blade force
F_{t}	N	Tangential blade force
L	N	Lift force
N_{b}	$-$	Number of blades
Q	Nm	Torque
r	m	Radial position of element
R	m	Blade radius
R_0	m	Root-cut-out radius
T_{Duct}	N	Duct thrust
T_{Fan}	N	Fan thrust
U	m/s	Resultant airspeed
U_{p}	m/s	Perpendicular airspeed
U_{t}	m/s	Tangential airspeed
v_{i}	m/s	Induced airspeed
$V_{\mathrm{x,y,z}}$	m/s	Ambient airspeed
α	rad	Aerodynamic angle of attack
θ	rad	Blade pitch angle
λ	$-$	Non-dimensional axial airspeed
λ_{i}	$-$	Non-dimensional induced airspeed
λ_{h}	$-$	λ_{i} in hover
$\mu_{\mathrm{x,y,z}}$	$-$	Non-dimensional ambient airspeed
ρ	kg/m^3	Air density
Φ	rad	Inflow angle
Ω	rad/s	Rotor speed

BEM	Blade Element Momentum
CFD	Computational Fluid Dynamics
CG	Center of Gravity
CS	Certification Specification
GW	Gross Weight
Hd	Density Altitude
HIGE	Hover In Ground Effect
HOGE	Hover Out of Ground Effect
Hp	Pressure Altitude
ISA	International Standard Atmosphere
LHD	Leonardo Helicopter Division
MTOW	Maximum Take Off Weight
NHEC	Non-Human External Cargo
nom	Nominal
NR	Rotor Speed
TT	Tension-Torsion
WAT	Weight Altitude Temperature

2 INTRODUCTION

A significant challenge in helicopter development remains the design, simulation, and testing of the tail rotor. These tasks become even more demanding with the implementation of a ducted tail rotor. While ducted tail rotors typically emit less noise, are safer for personnel on the ground, and can be more efficient due to the additional thrust produced by the duct [1–3], their aerodynamics is complex and difficult to model accurately, compared to open rotors. The ducted design can create intricate flow patterns, turbulence, and vortex interactions that are challenging to simulate, even with high-fidelity CFD calculations. This can make numerical simulations time-consuming and expensive, rendering them unsuitable for analyzing aircraft performance requirements, where several test conditions need to be evaluated quickly.

Alternatively, there are various low-order codes available, both open-source and commercial, which offer efficient and rapid calculations for static performance analysis. However, these codes face challenges when it comes to accurately incorporating flow separation phenomena and are restricted to axial flow scenarios [4]. As a consequence, addressing advanced flight conditions in the future demands substantial additional tuning efforts and a high level of customization. Recognizing these challenges, we decided to develop our own in-house rotor analysis tool, based on Blade Element Momentum (BEM) theory as described by Johnson [5], and leveraged the state-of-the-art capabilities of Kopter's Tail Rotor Test Rig to ensure appropriate tuning and calibration of our model.

The proposed method utilizes the thrust share factor, which represents the ratio of the fan thrust to the total thrust, along with free-stream correction factors in the induced inflow calculation of the shrouded rotor system. Unlike alternative models that rely on superposition with look-up tables to account for duct loads, this formulation offers significant advantages. The loads experienced by the duct are inherently dependent on the flight conditions and should not be extrapolated to hot and high conditions. Conversely, it is reasonable to assume that the ratio of fan thrust to total thrust remains consistent regardless of environmental conditions. However, it is worth noting that a comprehensive sensitivity study on this assumption is currently absent from the existing literature.

Johnson shows in Ref. [5], that for an ideal duct in hover, the far wake velocity is equal to the induced velocity at the rotor disk, and the thrust share factor becomes 1/2. This indicates an equal division of the total thrust between the fan and the duct. Conversely, a thrust share factor of unity corresponds to an open rotor configuration. As a result, the thrust share factor serves not only as a model parameter but also as an evaluative measure of the duct's effectiveness within the system.

To ensure an accurate representation of the duct effect, our first objective was to identify key parameters that influence system performance and, consequently, the thrust share factor. Among these parameters, a design element extensively examined in Refs. [6–9] is the gap between the blade tips and the inner surface of the duct. This gap plays a critical role in the airflow dynamics and the interaction between the rotor and the duct. A narrower tip gap minimizes leakage flow and enhances system efficiency, resulting in a lower thrust share factor. Stated differently, for the same total thrust, an increased tip gap necessitates a larger share of the fan's contribution, thereby requiring a higher thrust share factor for accurate system modeling.

Other important design parameters are the lip radius of the duct and the length and angle of its diffuser. Sometimes, the effects of the diffuser length and angle are collectively represented by the fan area expansion ratio to the diffuser's exit area. Pereira's study in Ref. [8] highlights that the performance of shrouded rotors deteriorates when the diffuser expansion ratio deviates from an optimal value. This deterioration can be attributed to flow separation occurring within the duct, downstream of the fan. Theoretically, a larger diffuser angle is advantageous as it reduces the contraction of the slipstream and, if feasible, even expands it. This leads to a decrease in the final wake velocity and an increase in the mass flow through the rotor, resulting in enhanced duct thrust and potentially reducing the thrust share factor. However, achieving this benefit is contingent upon avoiding the adverse pressure gradient in the diffuser that could induce separation of the slipstream from the duct geometry. Furthermore, it is worth noting that most design studies have primarily focused on shrouded rotors intended for UAV applications, where the duct length is significantly longer compared to a fan-in-fin configuration typically found in tail rotors.

In order to comprehensively analyze the factors influencing thrust share, it is essential to also consider operational parameters, including the axial airspeed, rotor speed, and the fan thrust setting. These parameters will be discussed in the subsequent section, drawing upon experimental data. Subsequently, the ducted BEM code incorporating thrust share information validated by experimental data is introduced. Finally, the presented rotor model is applied within a straightforward methodology, employed by the Flight Mechanics team at Kopter Group AG, to evaluate the pedal control margin during hover conditions, taking into account the effects of side winds. By integrating the aforementioned considerations, a comprehensive understanding of the thrust share dynamics and its impact on control performance can be achieved.

3 EXPERIMENTAL CAMPAIGN

The experimental campaign conducted on Kopter's tail rotor test rig aims to enhance our understanding of the factors influencing the thrust distribution between the fan and the total thrust. The investigation focuses on three key factors: rotor speed, axial airspeed, and the tip gap between the rotor blades and the duct. By examining these factors, we seek to gain valuable insights into the complex dynamics that govern thrust allocation in the tail rotor system. This knowledge will contribute to the optimization and refinement of the system's performance and efficiency, as well as to its modeling approach.

3.1 Experimental Set-up

In recent years, Kopter has gained valuable knowledge in the field of ducted rotors, leveraging its expertise by developing and utilizing a dedicated test bench (Figure 1). This advanced test rig incorporates a range of cutting-edge sensors and instrumentation to accurately measure the loads acting upon both the rotor and shroud. To capture the forces and moments experienced during operation, strain gauges, load cells, and accelerometers are strategically positioned along the rotor and shroud structure. Real-time data from these sensors provide precise measurements of the loads, facilitating comprehensive analysis and evaluation.

Figure 1: Rear view of the tail rotor test rig.

The outcomes of extensive measurement campaigns conducted in the past yield valuable insights into the influence of operational parameters, such as rotor speed and axial airspeed, on the distribution of thrust between the fan and the overall system of the AW09 tail rotor. Additionally, these measurement campaigns serve as a crucial validation benchmark for the BEM code, ensuring the accuracy and reliability of the computational model.

3.2 What Affects the Thrust Share?

The thrust share factor, represented by Equation 1, quantifies the proportion of thrust contributed by the fan in relation to the total thrust generated.

$$f_T = \frac{T_{\text{Fan}}}{T_{\text{Fan}} + T_{\text{Duct}}} \quad (1)$$

In the upcoming sections, we analyze how the tip gap, rotor speed, and axial airspeed affect this factor.

3.2.1 Tip Gap

The effect of the tip gap on rotor performance was investigated by measuring the loads on the duct and fan with both nominal and shortened blades. This resulted in a doubling of the tip gap, referred to as the "large tip gap" in the subsequent graphs, in comparison to the "small tip gap" of the nominal configuration.

Figure 2 illustrates the comparison of the thrust share factor between the two tip gap configurations. The graph clearly demonstrates that increasing the distance between the blades and the shroud reduces the rotor's efficiency, as indicated by the increased thrust share of the fan. This observation aligns with the findings in the existing literature. A higher thrust share for the same C_T signifies an increased contribution of the fan to the total thrust, consequently requiring more power to satisfy the same anti-torque demand.

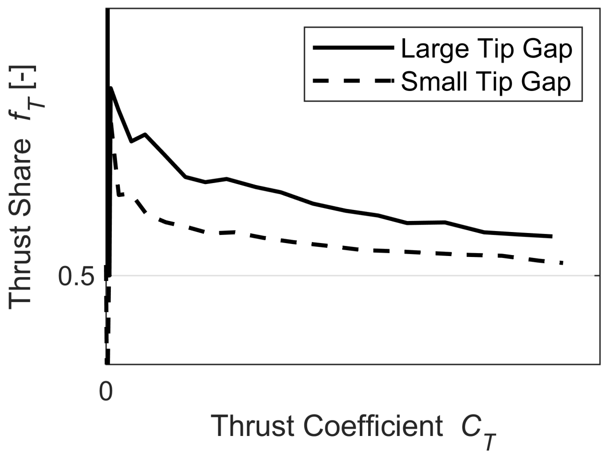

Figure 2: Difference in the thrust share factor due to an increased tip gap.

Figure 3 and Figure 4 emphasize that the change in the relationship between fan thrust and total thrust stems from alterations in the load on the duct. The fan thrust remains nearly unaffected by the distance to the duct, whereas the duct generates greater thrust for the smaller tip gap. From the perspective of pedal control margins, this implies that a smaller tip gap offers advantages as it generates more thrust through the non-rotating part of the rotor for the same pedal position. Consequently, less pedal control is necessary to meet the same anti-torque demand.

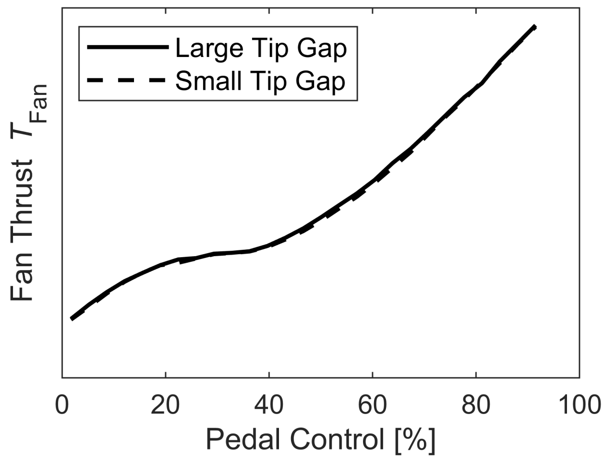

Figure 3: Difference in the fan thrust due to an increased tip gap.

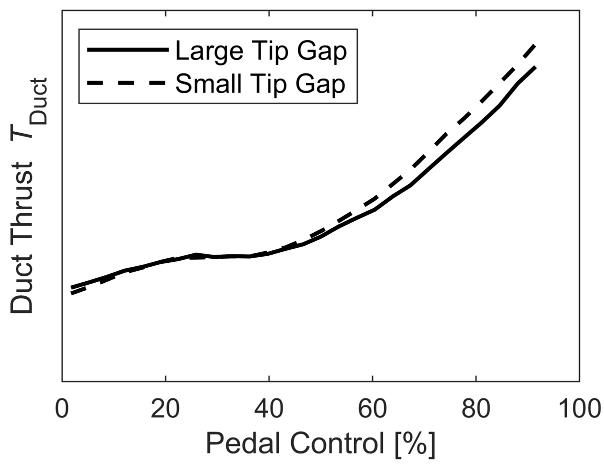

Figure 4: Difference in the duct thrust due to an increased tip gap.

3.2.2 Rotor Speed

Figure 5 presents the relationship between the thrust share and the thrust coefficient of the rotor system, encompassing the fan and duct, while maintaining a constant rotor speed. The graph indicates that as the thrust coefficient increases, the thrust share decreases, implying a reduction in the fan's contribution to the overall load. Notably, the lowest speed setting exhibits higher thrust share values than the higher speed settings, but no clear trend emerges with increasing rotational speed. Overall, the thrust share remains relatively independent of the rotor speed within the typical range for helicopter applications.

This characteristic is particularly significant in the high-thrust region, which is crucial for assessing the control margin of the tail rotor. Within this region, the spread in measurements decreases, and the thrust share approaches its theoretical maximum, irrespective of the rotor speed.

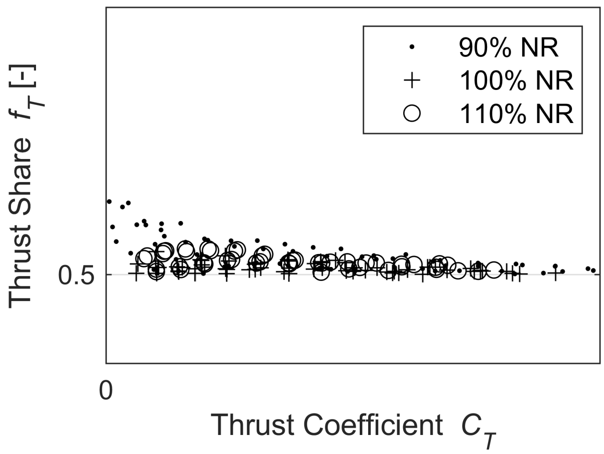

Figure 5: Thrust share factor at constant rotor speeds.

These observations deviate somewhat from the findings in existing literature, albeit predominantly focused on small ducted rotors for UAV applications with a fixed pitch and, consequently, greater range in NR. Reference [6] suggests that at low RPM, the viscous losses in the internal flow of the duct can counteract the duct's thrust, potentially compromising the system's performance. However, for our rotor, this behavior is only evident for thrust coefficients close to zero, where the thrust share factor is noticeably larger in the low-speed setting.

3.2.3 Axial Airspeed

Rotorcraft performance requirements in hover typically involve operating conditions with side wind in the direction opposite of the tail rotor thrust. This axial airspeed causes a reduction of the angle of attack of the fan blades, necessitating higher blade pitch and pedal commands compared to windless conditions, as the rotor is effectively experiencing a climb condition. Hence, to ensure sufficient yaw control authority during hover, assessing whether the available pedal range remains adequate in the presence of substantial side wind components is crucial. In addition to reducing the fan's thrust, the profile drag of the shroud increases, counteracting its thrust and effectively diminishing the total thrust of the system. Consequently, this can compromise the directional stability during hover. A study conducted by Roh et al. [10] confirms that this effect is particularly significant when the airspeed component aligns axially with the tail rotor, opposing its thrust vector.

The impact of this phenomenon on the thrust share was investigated experimentally by colleagues from Leonardo's Helicopter Division (LHD) using a similar ducted tail rotor design. The results in Figure 6 indicate that an increase in axial speed causes a rise in the thrust share factor at a constant thrust coefficient. This can be attributed to the effective reduction in duct thrust caused by additional profile drag and the decrease in fan thrust at a constant blade pitch. Consequently, in order to maintain yaw stability, the fan thrust must increase, thus leading to a greater thrust share factor. Interestingly, the thrust share factor can even surpass unity if the aerodynamic force of the duct results in a negative duct thrust without exceeding the fan thrust in an absolute sense.

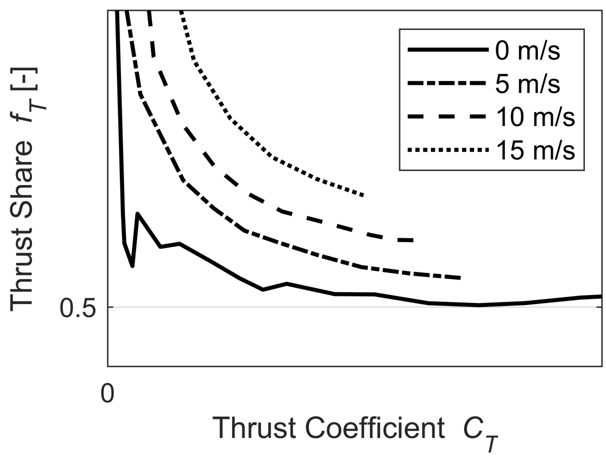

Figure 6: Thrust share factor at constant axial airspeeds.

In summary, the empirical data suggests that the distribution of thrust between the fan and fan-duct system depends not only on the tip gap but also on the axial airspeed and total rotor thrust, rather than on its rotational speed. These discoveries are integrated into the subsequent sections' BEM model by defining the thrust share factor as a function of the total thrust and axial airspeed for a fixed rotor configuration.

4 AW09 DUCTED TAIL ROTOR MODEL

This section describes the rotor system and presents a detailed examination of the developed rotor model, followed by a thorough validation process. The system description is given in Section 4.1. The model's components and parameters are described in Section 4.2, while the subsequent Section 4.3 focuses on validating the model through both test bench experiments and flight tests.

4.1 System Description

The ducted tail rotor system comprises ten non-uniformly distributed blades and rotates in a clockwise direction. Blade pitch adjustment is achieved mechanically through a spider mechanism that connects the pitch control shaft to the blade holders. The transfer of centrifugal loads between the blade holder and the rotor head is facilitated by Tension-Torsion (TT) Straps. These straps not only provide a structural connection but also enable controlled torsional motion, functioning as torsion hinges. This system design ensures precise control over blade pitch and effective load transfer, contributing to the overall performance and stability of the ducted tail rotor.

4.2 Model Description

The ducted rotor BEM model extends the conventional BEM formulation to account for the influence of the duct on the total thrust and the airspeed at the rotor disk. The model incorporates the calculation of airspeed, elemental forces, and the integration of these forces to obtain the total thrust. Additionally, the thrust share factor is introduced to determine the individual thrust contributions of the fan and the duct, and free-stream correction factors are used to account for the acceleration or deceleration of the air through the duct.

Similar to a conventional BEM model, the airspeed at each element is determined from the rotational speed of the rotor and the inflow induced by the rotor's own slipstream, with the addition of the velocity of the free-stream air affected by the duct through correction factors. The resultant airspeed, denoted as U, is given by the vector sum of the perpendicular (U_p) and the tangential (U_t) speed, as described below:

$$U_\mathsf{p} = \kappa v_\mathsf{i} + f_{V_\mathsf{z}} V_\mathsf{z} \tag{2}$$

$$U_\mathsf{t} = \Omega r + f_{V_\mathsf{x}} V_\mathsf{x} + f_{V_\mathsf{y}} V_\mathsf{y} \tag{3}$$

$$U = \sqrt{U_\mathsf{p}^2 + U_\mathsf{t}^2} \tag{4}$$

$$\Phi = \tan^{-1}(U_\mathsf{p}/U_\mathsf{t}) \tag{5}$$

where v_i is the induced airspeed, $V_\mathsf{x,y,z}$ are the free-stream velocity components, Ω is the angular speed of the blade with the radial vector r, and $f_{V_\mathsf{x,y,z}}$ are the free-stream correction factors due to the presence of the duct. Additionally, an empirical correction factor κ is used to account for the swirl in the wake, tip vortices, and non-uniformity in the inflow. The angle of attack α of a blade element is then calculated by the difference between its local pitch θ and inflow angle Φ as $\alpha = \theta - \Phi$.

To calculate the elemental forces of the fan, the BEM model employs the blade element theory, which assumes that the lift (L) and drag (D) forces acting on each element can be resolved into axial and tangential components. The axial force, denoted as F_n, contributes to the thrust, while the tangential force, denoted as F_t, accounts for torque:

$$L = 1/2 \rho U^2 c c_l \tag{6}$$

$$D = 1/2 \rho U^2 c c_d \tag{7}$$

$$F_\mathsf{n} = L\cos(\Phi) - D\sin(\Phi) \tag{8}$$

$$F_\mathsf{t} = L\sin(\Phi) + D\cos(\Phi) \tag{9}$$

where ρ is the air density and c is the blade chord. The lift and drag coefficients for each element are determined based on airfoil characteristics, angle of attack, and Mach number.

The total thrust and torque of the fan denoted as T_Fan and Q, respectively, are given by integration of the elemental forces over the blade span, averaging over the azimuth, and multiplying it with the number of blades N_b:

$$T_\mathsf{Fan} = \frac{N_\mathsf{b}}{2\pi} \int_0^{2\pi} \int_{R_0}^{R} F_\mathsf{n} \cdot dr \cdot d\psi \tag{10}$$

$$Q = \frac{N_\mathsf{b}}{2\pi} \int_0^{2\pi} \int_{R_0}^{R} F_\mathsf{t} r \cdot dr \cdot d\psi \tag{11}$$

where R_0 is the root-cut-out radius and R the radius of the fan. Finally, the duct thrust is determined with the thrust share factor, while the overall system thrust (T) of the rotor is the sum of the fan and duct thrust contributions:

$$T_{\mathsf{Duct}} = T_{\mathsf{Fan}}(1/f_T - 1) \tag{12}$$

$$T = T_{\mathsf{Fan}} + T_{\mathsf{Duct}} \tag{13}$$

The presented calculation of the rotor loads necessitates an iterative process due to the interdependencies between the induced inflow v_{i}, the thrust share factor f_T, and the rotor thrust T. The thrust share factor can be updated from an initial guess straightforwardly using look-up tables from experimental data. To determine the induced inflow, an extended momentum theory formulation, based on Glauert's inflow formula for open rotors (Eqn. 14), as outlined by Johnson in Ref. [5], is employed. This formulation is given in Equation 15, and can be solved similarly to the open rotor formulation by substituting $f_{V_{\mathsf{z}}}\mu_{\mathsf{z}} + \lambda_{\mathsf{i}}$ for λ, $\lambda_{\mathsf{h}}^2/f_T$ for λ_{h}^2, $f_{V_{\mathsf{x}}}\mu_{\mathsf{x}}$ for μ_{x}, $f_{V_{\mathsf{y}}}\mu_{\mathsf{y}}$ for μ_{y}, and μ_{z}/f_T for μ_{z}.

$$\lambda = \frac{\lambda_{\mathsf{h}}^2}{\sqrt{\lambda^2 + \mu_{\mathsf{x}}^2 + \mu_{\mathsf{y}}^2}} + \mu_{\mathsf{z}} \tag{14}$$

$$f_{V_{\mathsf{z}}}\mu_{\mathsf{z}} + \lambda_{\mathsf{i}} = \frac{\lambda_{\mathsf{h}}^2/f_T}{\sqrt{(f_{V_{\mathsf{z}}}\mu_{\mathsf{z}} + \lambda_{\mathsf{i}})^2 + (f_{V_{\mathsf{x}}}\mu_{\mathsf{x}})^2 + (f_{V_{\mathsf{y}}}\mu_{\mathsf{y}})^2}} + \frac{\mu_{\mathsf{z}}}{f_T} \tag{15}$$

The variables $\mu_{\mathsf{x,y,z}}$ and λ_{i} are the airspeed components $V_{\mathsf{x,y,z}}$ and the induced inflow v_{i}, non-dimensionalised by the tip speed ΩR, respectively. The variable $\lambda_{\mathsf{h}}^2 = C_T/2$ is the non-dimensional inflow in hover.

The inflow equation (15) is solved iteratively using the secant method until the change in λ_{i} between consecutive iterations falls below a predefined threshold. The model offers the flexibility to calculate the inflow either uniformly or with a radial distribution. In the case of uniform inflow, the thrust coefficient $C_T = T/(\rho A(\Omega R)^2)$ is computed as a scalar using the total thrust. However, when considering a radial inflow distribution, the thrust coefficient is determined for each radial annulus using the equation:

$$C_T(r) = \frac{\tilde{T}_{\mathsf{Fan}}(r)/f_T}{\rho A(r)(\Omega R)^2} \tag{16}$$

Here, $\tilde{T}_{\mathsf{Fan}}(r)$ represents the radial distribution of the fan thrust, while $A(r)$ denotes the area of each annulus.

4.3 Model Validation

The following sections present the validation of the BEM model by comparing rotor polars and inflow calculations with experimental data obtained from the test bench and flight test. Two inflow models, namely the uniform and annular inflow models, are examined to evaluate their impact on rotor performance. By validating the tail rotor model through meticulous analysis of ground and flight test data, we can enhance our understanding of tail rotor dynamics, refine model predictions, and ultimately advance the design and operation of rotorcraft systems. The findings from this validation process will contribute to more accurate simulations, leading to improved helicopter performance, maneuverability, and safety during hover and, low-speed and high-speed flight in the future.

4.3.1 Test Bench

The performance characteristics of the proposed inflow models are visually presented in Figures 7, 8, and 9, showcasing their effectiveness across a range of operating conditions. The tuning of the model involved a hub drag correction to increase the torque at zero thrust, a tip loss correction to decrease the lift near the blade tip, and an adjustment of the inflow correction factor κ to modulate the induced velocity.

Precise calculations of rotor thrust, power, and the Figure of Merit have been achieved by establishing a functional relationship between κ and total thrust. Notably, different κ-values were determined for the uniform inflow model and the annular inflow model. Specifically, the κ-values associated with the annular inflow model were found to be lower, aligning with the expectation that an annular inflow distribution better represents real flow conditions compared to a uniform assumption. As a result, the need for manual tuning through a correction factor is reduced.

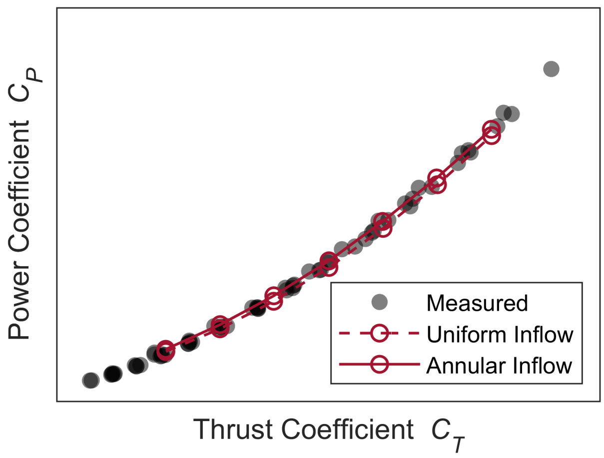

Figure 7: Power and thrust coefficient comparison between measured and calculated data for the uniform and annular inflow model.

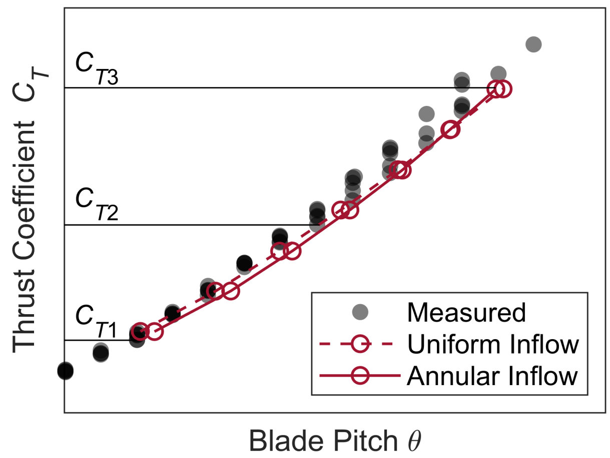

Figure 9: Thrust coefficient and blade pitch comparison between measured and calculated data for the uniform and annular inflow model. Horizontal lines indicate the thrust settings for the inflow comparison in Figure 10.

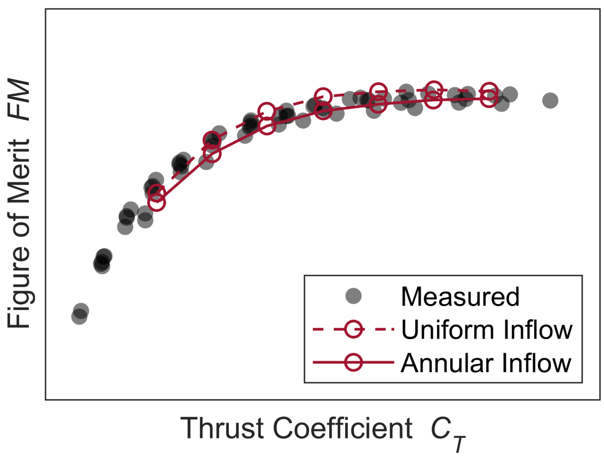

Figure 8: Figure of Merit and thrust coefficient comparison between measured and calculated data for the uniform and annular inflow model.

The resulting thrust polar graph depicted in Figure 9 effectively encompasses the measured data points from the right. Consequently, this conservative estimation of blade pitch for achieving the desired rotor thrust establishes a safety margin for subsequent assessments of control authority.

In the course of the experimental campaign described in Section 3, inflow profiles were measured with a five-hole probe along the fan radius at the three thrust settings ($C_{T1} - C_{T3}$) indicated in Figure 9.

To ensure safety and minimize flow disruption, the inflow was assessed using a calibrated five-hole probe positioned along the blade radius immediately behind the rotor disk. By systematically traversing the probe along the rotor radius, numerous data points can be collected, facilitating the creation of a two-dimensional representation of the flow condition. The probe captures static pressures at its five holes, enabling conversion into flow angles and velocities utilizing predetermined calibration coefficients. However, it is important to note that the inflow at the rotor needs to be deduced from the dynamic pressure or by considering the vector sum of the flow components, as the pressure measurements are obtained behind the rotor disk.

Despite the rotor polars demonstrating excellent agreement, the inflow profiles depicted in Figure 10 display small discrepancies, with an overestimation of induced velocity in the high thrust region and an underestimation in the low thrust region. These differences arise from the variation of κ with thrust, which is necessary to achieve the desired shape of the thrust polar and ensure compatibility with the Figure of Merit. While an exact match in the inflow could be attained with a constant inflow correction factor, it would compromise the Figure of Merit. A remedy that could be considered for future development is an additional degree of freedom by implementing another tuning factor modulating the profile drag of the blade. This should affect the required torque and, hence, power as well as the Figure of Merit, without changing the inflow.

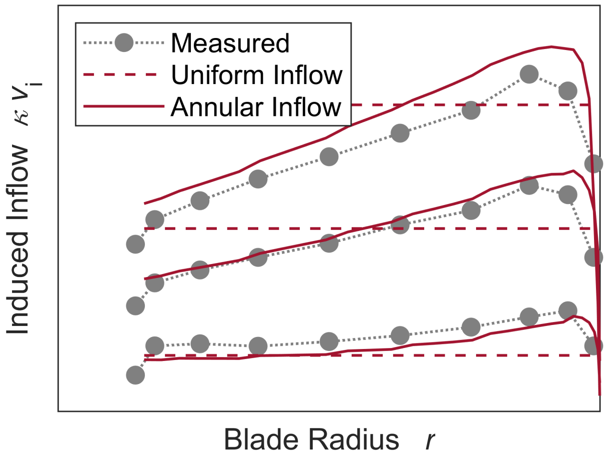

Figure 10: Induced inflow distribution comparison between measured and calculated data for the uniform and annular inflow model at the thrust settings indicated in Figure 9.

For the estimation of yaw authority, the accuracy of the relationship between rotor thrust and blade pitch is of utmost importance. Considering the inherent uncertainty resulting from relatively high noise in the inflow measurement, the model behavior presented in this section is deemed sufficiently accurate for both inflow models. Nonetheless, in the subsequent analyses, we will proceed with the annular inflow model, as it qualitatively represents the inflow profile better and necessitates lower correction factors while maintaining comparable computational efficiency.

4.3.2 Flight Test

This section is dedicated to the validation of the tail rotor model in the hover regime, utilizing flight test data obtained from the latest AW09 pre-series prototype. The validation process involves comparing the outputs of the tail rotor model, including thrust, power requirements, and control inputs, with the corresponding data acquired in flight.

In the flight test scenario, direct measurement of tail rotor forces is not feasible. Instead, the tail rotor torque, and therefore power, is available. To determine the thrust of the tail rotor during hovering flight without wind, the measured main rotor torque and the moment arm of the tail are used. Then, a trim calculation is performed using the BEM code to estimate the required power and blade pitch numerically. Finally, the pedal control demand is derived by applying the appropriate rigging law.

Figure 11 demonstrates that similar to the test bench results, the model accurately calculates the required power for a given thrust in flight. This was anticipated, considering the identical installation of blades and the replication of the AW09 fin duct on the test bench. Although the tip gap on the flying prototype is slightly larger than on the test bench, it seems small enough to not impact the relationship between thrust and power.

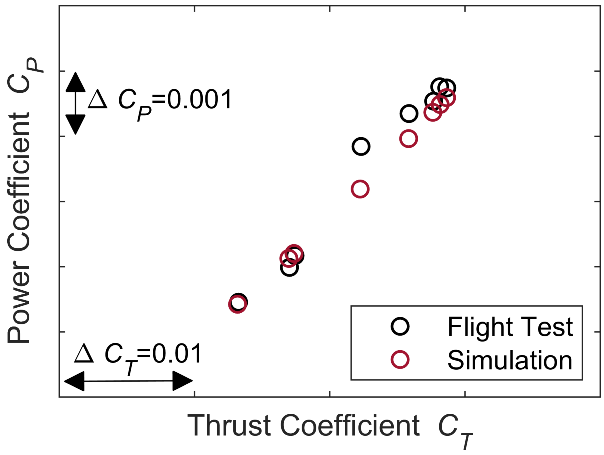

Figure 11: Comparison of measured and simulated data for power and thrust coefficient in hover.

A comparison of the pedal command in Figure 12, however, reveals an offset between the flight test and simulation data. In the simulation, the pedal control is generally lower than the measured value for the same thrust coefficient. This disparity can be partially attributed to the larger tip gap, as described in Section 3.2.1, but it is primarily due to flexibility in the control chain between the fan blades and the pedals. The simulation model assumes rigid controls and employs a linear rigging law, whereas, in reality, the control components possess a degree of flexibility. Consequently, the actual pedal control demand is greater than that predicted by the rigid model. In our specific case, this flexibility results in a shift in pedal control of approximately 2.5%.

To improve accuracy, this delta will be incorporated into the results of the subsequent control authority assessment.

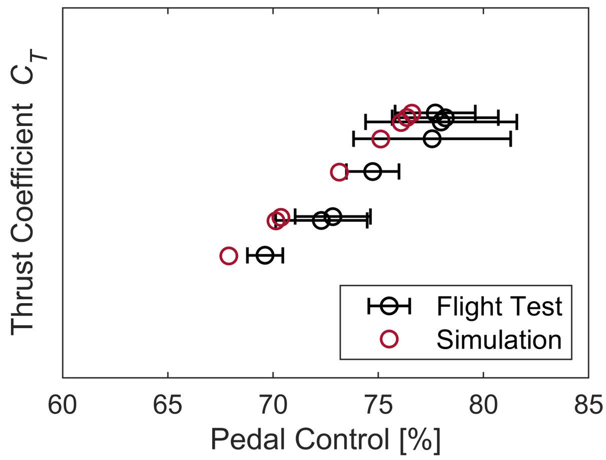

Figure 12: Comparison of measured and simulated data for thrust coefficient and pedal command in hover.

To validate the model under axial flight conditions, preliminary results from three left quartering flights are utilized to emulate a hovering scenario with side wind opposing the tail rotor thrust. In this flight configuration, the tail rotor must generate additional thrust to compensate for the drag produced by the vertical fin. Simultaneously, the main rotor torque is expected to decrease due to reduced induced power during translatory flight, resulting in a lower anti-torque demand for the tail rotor. Consequently, determining the tail rotor thrust requirement solely based on its moment arm and the main rotor torque is not adequate.

To address this, a FLIGHTLAB full aircraft trim calculation is employed using the validated AW09 model to accurately determine the tail rotor thrust during hover with side wind. The comprehensive full aircraft model demonstrates high accuracy in simulating the main rotor torque within this flight regime and incorporates aerodynamic panels with wind tunnel test data specifically for the vertical fin. As a result, the model proves highly reliable in calculating the tail rotor thrust, ensuring the accuracy and effectiveness of the validation process.

The subsequent figures present a comparison between flight test data and simulation data for the power coefficient, thrust coefficient, and pedal control during low-speed flights to the left.

It is worth noting that the thrust coefficients labeled as ”Flight Test” are calculated using the previously mentioned FLIGHTLAB model, whereas the power coefficient and pedal control were directly measured during flight. To achieve a suitable alignment in pedal control (Figure 13) and power demand (Figure 14) between the flight test and BEM simulation data, the inflow correction factor had to be increased. This finding underscores an additional dependency of the inflow correction on the free-stream velocity, in addition to the thrust and inflow model.

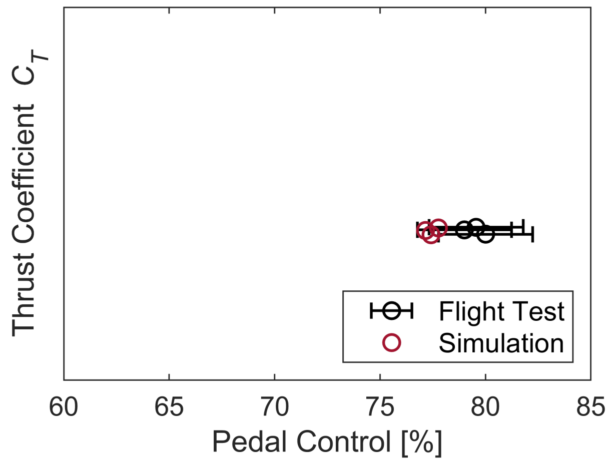

Figure 13: Comparison of measured and simulated data for thrust coefficient and pedal command in sideward flight.

By increasing the inflow correction factor, the power demand of the rotor is amplified due to an increased induced drag on the blades. At the same time, the greater inflow reduces the angle of attack at the blades, necessitating a more substantial blade pitch and subsequently leading to a higher pedal control requirement. Through this systematic approach, the power and pedal demand of the rotor were incrementally raised until an offset in the pedal control (as depicted in Figure 13) similar to the hovering case was observed, attributed to the flexibility of the control chain.

Nevertheless, Figure 14 illustrates that the simulation tends to underestimate the tail rotor power in the presence of side wind. This discrepancy can be attributed to two primary reasons. Firstly, the simulation assumes an ideal duct with a perfectly axial and clean free-stream velocity, denoted by $f_{V_x} = 0$, $f_{V_y} = 0$, and $f_{V_z} = 1$.

However, in reality, this is not the case. Even when the helicopter flies at a perfect 90-degree angle to the left, its roll attitude creates an angle between the airspeed and shaft axis. Additionally, aerodynamic interference between the rotor and other components, such as the fin and tail boom, affects the inflow to the fan and consequently impacts its performance.

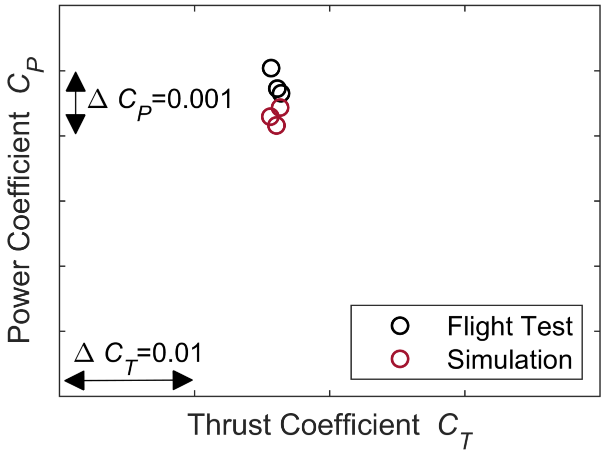

Figure 14: Comparison of measured and simulated data for power and thrust coefficient in sideward flight.

Overcoming these limitations would require adapting the free-stream correction factors $f_{V_{x,y,z}}$ and additional tuning efforts to accurately represent the flow conditions. However, obtaining extensive flow field data, either through experiments or numerical simulations, is necessary for this purpose.

Secondly, an underestimated power demand can be representative of a low thrust share factor as less of the total thrust is delivered by the fan in the simulation compared to the flight test. When the fan assumes a lower thrust share while maintaining the same total thrust, it requires a smaller blade pitch, resulting in reduced power demand. This observation suggests that the dependency of the thrust share factor on the axial airspeed, as employed in our model from Section 3.2.3, may be too low.

Despite the limited available test data, the model exhibits consistent behavior in both wind and no-wind conditions. The validation exercises demonstrate the simulation model's ability to accurately capture the physics of the isolated rotor and effectively simulate pedal control for the full aircraft. Through comparisons with flight test data, it was identified that a necessary adjustment in pedal demand is required to account for the flexibility in the control chain. Implementing this offset enhances the accuracy of subsequent control margin assessments and provides an additional safety margin.

5 CONTROL AUTHORITY ASSESSMENT

The control authority evaluation of the AW09 ducted tail rotor involves simulating the pedal demand at specific requirement points and assessing the margin to its full deflection. These requirement points are determined based on the Certification Specification (CS) and strategic hover performance requirements. To ensure controllability and maneuverability, the CS specifies three requirements in CS 27.143 (c) and (d) for hover in and out of ground effect. These points are summarized in the first three lines of Table 1, with "WAT" representing the maximum feasible take-off weight obtained from the Weight Altitude Temperature (WAT) hover performance chart. Additionally, the lower limit NR is selected whenever the CS requires a critical rotor speed, while the nominal (nom) NR is used otherwise.

Table 1: Tail rotor control authority requirement points from CS 27.

#	Type	Hd	GW	NR	Wind
1	HIGE	7000 ft	MTOW	low	17 kts
2	HIGE	13500 ft	WAT	low	17 kts
3	HOGE	13500 ft	WAT	nom	17 kts
4	HOGE	4991 ft	MTOW	nom	0 kts

The wind component is directed opposite to the tail rotor thrust. All the requirements refer to a rear CG configuration, as it provides the lowest arm for the tail rotor thrust and hence, is the most demanding. The fourth requirement point in Table 1 is derived from CS 27.49(a), which outlines a performance requirement at 2500 ft pressure altitude ISA+22. Its inclusion in this table ensures comprehensive coverage of the evaluation.

The simulation procedure is divided into two distinct phases, as illustrated in Figure 15. In the first phase, the anti-torque demand is determined through a comprehensive helicopter trim simulation specifically focused on hover conditions. Subsequently, in the second phase, the tail rotor is trimmed based on the predicted thrust level.

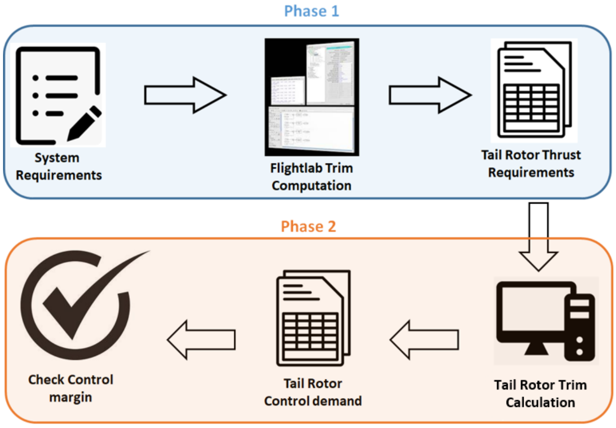

Figure 15: Methodology of the control authority assessment.

To accomplish these phases, different software tools are utilized. The initial analysis phase relies on the FLIGHTLAB software, a well-validated tool extensively employed for full helicopter simulations at Kopter. FLIGHTLAB is capable of accurately calculating the main rotor torque, thereby providing precise tail rotor thrust demand estimations, even in the presence of side wind. For the second phase, the ducted rotor BEM tool is employed, leveraging its specific tuning to the AW09 tail rotor. This procedure allows us to assess pedal demand with a high level of accuracy in scenarios where test data is unavailable.

Figure 16 displays the observed pedal control demand, revealing the presence of sufficient pedal control across all CS-mandated points. It is worth noting that the self-imposed safety margin of 10% is only minimally approached in the most demanding requirement point. This margin ensures adequate control authority, even during transient periods of intensified side wind, such as gusts. Moreover, it facilitates the possibility of accommodating aircraft growth and meeting more rigorous operational requirements.

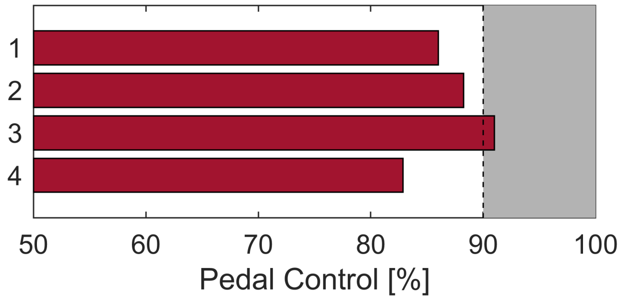

Figure 16: Pedal control demand in the CS 27 requirement points of Table 1.

In addition to conforming to the specifications set forth by the CS, Kopter has established strategic hover requirements for the entire aircraft. Table 2 provides an overview of a subset of these full aircraft requirement points, which are then translated into corresponding tail rotor thrust demands, considering both the presence and absence of side wind.

Table 2: Additional strategic tail rotor requirement points.

#	GW	Hp	ISA	Wind
5	WAT	15780 ft	0	0 kts
6	WAT	4000 ft	+25	0 kts
7	WAT	14500 ft	0	0 kts
8	NHEC1	4000 ft	+20	0 kts
9	NHEC2	8000 ft	+20	0 kts
10	NHEC3	0 ft	+30	0 kts
11	NHEC4	8000 ft	+30	0 kts

These requirements encompass challenging scenarios such as hot and high environmental conditions as well as an increased gross weight resulting from Non-Human External Cargo (NHEC) operations.

The combination of hot and high conditions, along with a high take-off weight, presents a particularly demanding situation. In such cases, the anti-torque demand is substantial while the aerodynamic force generated by the tail rotor blade is reduced due to the high main rotor torque and low air density, respectively.

The availability of a safe pedal control margin for all specified conditions is demonstrated in Figure 17 and a robust safety margin of at least ten percent is consistently maintained.

These observations highlight the ability to maintain a reliable anti-torque force under a wide range of operational conditions.

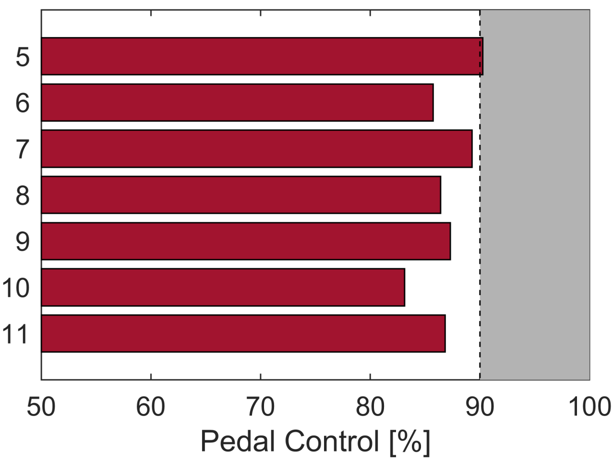

Figure 17: Pedal control demand in the strategic requirement points of Table 2.

6 CONCLUDING REMARKS

This study has presented a comprehensive analysis of the control authority and performance of the AW09 ducted tail rotor system. Through rigorous simulations and evaluations, we have assessed the pedal control capabilities of the system, both in accordance with the Certification Specification requirements and Kopter's strategic hover performance standards. The results have demonstrated that the AW09 ducted tail rotor exhibits sufficient pedal control in all mandated points, even when subjected to challenging conditions such as side wind and high take-off weights.

Furthermore, the evaluation of the system's performance under various operational scenarios, including hot and high environmental conditions and the presence of Non-Human External Cargo (NHEC), has revealed the robustness and reliability of the tail rotor system. The ample pedal control observed throughout these scenarios confirms the system's stability and ability to maintain control authority even in demanding situations.

It is important to note that this study has been conducted using validated software tools, such as FLIGHTLAB and the in-house BEM tool, ensuring accuracy and reliability in the analysis. The use of these tools, along with the adherence to industry standards and requirements, strengthens the confidence in the obtained results and their applicability to real-world operational scenarios.

Overall, the findings of this study provide valuable insights into the control authority and performance of the AW09 ducted tail rotor system. The knowledge gained from this analysis can be utilized to enhance the design and operation of future rotorcraft systems, improving safety, maneuverability, and overall performance.

Future work will focus on expanding the analysis to include additional operating conditions and factors that may impact control authority, most importantly wind speeds from all azimuths. Additionally, experimental validation of the simulation results through the ongoing flight test campaign will further strengthen the confidence in the findings and provide a more comprehensive understanding of the system's capabilities. The ongoing development of the in-house BEM tool will involve incorporating 2D maps for the free-stream correction factors. This enhancement aims to improve the simulation capabilities for hovering flight with side wind and potentially extend to forward flight scenarios.

Soeren.Boelk@koptergroup.com
Alessandro.Masi@contractor.koptergroup.com
Francesco.Scorcelletti@koptergroup.com

ACKNOWLEDGMENT

We would like to extend our sincere thanks to our colleagues at LHD for sharing the experimental dataset and providing valuable support in studying the tail rotor. Their contributions have played an important role in the development of this activity. We also want to express our appreciation to the Kopter Experimental Team for setting up the bench and assisting us in obtaining the experimental data. Their efforts have been instrumental in the success of our research project.

REFERENCES

[1] Kruger, W., “On wind tunnel tests and computations concerning the problem of shrouded propellers,” Tech. Rep., 1949.

[2] Platt Jr, R. J., “Static tests of a shrouded and an unshrouded propeller,” Tech. Rep., 1948.

[3] Yilmaz, S., Erdem, D., and Kavsaoglu, M., “Effects of duct shape on a ducted propeller performance,” in *51st AIAA aerospace sciences meeting including the new horizons forum and aerospace exposition*, 2013, p. 803.

[4] Zhang, T. and Barakos, G. N., “Review on ducted fans for compound rotorcraft,” *The Aeronautical Journal*, vol. 124, no. 1277, pp. 941–974, 2020.

[5] Johnson, W., *Rotorcraft aeromechanics*. Cambridge University Press, 2013, vol. 36.

[6] Martin, P. and Tung, C., “Performance and flowfield measurements on a 10-inch ducted rotor vtol uav,” Army Research Development and Engineering Command Moffett Field CA Aviation Aeroflight Dynamics Directorate, Tech. Rep., 2004.

[7] Akturk, A. and Camci, C., “Tip clearance investigation of a ducted fan used in vtol uavs: Part 1—baseline experiments and computational validation,” in *Turbo Expo: Power for Land, Sea, and Air*, vol. 54679, 2011, pp. 331–344.

[8] Pereira, J. L. and Chopra, I., “Hover tests of micro aerial vehicle-scale shrouded rotors, part i: Performance characteristics,” *Journal of the American Helicopter Society*, vol. 54, no. 1, pp. 12 001–12 001, 2009.

[9] Pereira, J. L. and Chopra, I., “Hover tests of micro aerial vehicle-scale shrouded rotors, part ii: Flow field measurements,” *Journal of the American Helicopter Society*, vol. 54, no. 1, pp. 12 002–12 002, 2009.

[10] Roh, N., Oh, S., and Park, D., “Aerodynamic characteristics of helicopter with ducted fan tail rotor in hover under low-speed crosswind,” *International journal of aerospace engineering*, vol. 2020, pp. 1–14, 2020.